

Dipole Pattern of Meridional Atmospheric Internal Energy Transport Across the Arctic Gate

Mikhail M. Latonin (✉ m.m.latonin@spbu.ru)

Saint Petersburg State University

Leonid P. Bobylev

Nansen International Environmental and Remote Sensing Center

Igor L. Bashmachnikov

Saint Petersburg State University

Richard Davy

Bjerknes Centre for Climate Research

Research Article

Keywords: Dipole pattern, atmospheric internal energy, transport, Arctic gate, numerous studies, Western Hemisphere

Posted Date: September 24th, 2021

DOI: <https://doi.org/10.21203/rs.3.rs-764400/v1>

License:   This work is licensed under a Creative Commons Attribution 4.0 International License.

[Read Full License](#)

Version of Record: A version of this preprint was published at Scientific Reports on February 11th, 2022. See the published version at <https://doi.org/10.1038/s41598-022-06371-9>.

Abstract

High-latitude atmospheric meridional energy transport plays a fundamental role in the Arctic climate system. However, despite numerous studies, there are no established clear regional features of the atmospheric energy transport components from a large-scale perspective. This study aims at investigating the internal energy and its instantaneous sensible and latent heat transports in the troposphere through the Arctic gate at 70°N using the high-resolution climate reanalysis ERA5. We have done a regional analysis of the time series of heat fluxes across the zonal section and found by decomposing them into the empirical orthogonal functions that they have opposing features for the Eastern and Western Hemispheres. In particular, the sensible heat transport dominates in the Western Hemisphere, whereas the latent heat transport dominates in the Eastern Hemisphere. Moreover, we detected the existence of an anti-phase dipole pattern for each of these components in the entire troposphere, which is robust because it was retained during both the climate cooling in 1950–1978 and warming in 1979–2019. The hemispheric net fluxes indicate that the Arctic gains internal energy mostly due to the latent heat transport.

Introduction

Atmospheric meridional energy transport (AMET) can be decomposed into internal energy transport (sensible and latent heat fluxes), potential and kinetic energy transports. The latter component is often disregarded due to its negligible contribution^{1,2}. The remaining components are often referred to as the moist static energy transport^{3,4}. In turn, each of them consists of transient eddies, stationary eddies, mean meridional circulation and net mass flow^{3,5}. The latter term must tend to zero at monthly and longer time scales to fulfill the mass conservation law⁶. However, there is no conventional way for computing AMET. One of the reasons for that is a desire to obtain a value with a specific unit of measurement, such as corresponding to the specific humidity for moisture transport, by applying different normalisations and weights^{5,7,8,9}.

Despite some discrepancies in the methodologies, important pathways and sources of AMET relevant for the Arctic have previously been identified, which are mostly the oceanic areas in the North Atlantic and North Pacific during the cold season^{10,11} and continental areas in Eurasia and North America during the warm season, especially for the latent heat component of the internal energy^{12,13}. The AMET is most often calculated at the 70°N parallel, because this is a region of strong influence of the polar vortex¹⁴, and Bjerknes compensation is strongest at this latitude¹⁵.

Among the AMET and its internal energy components, the latent heat flux into the Arctic is of the highest interest as it initiates a regional feedback by increasing the downward longwave radiation, and has a further potential of melting the Arctic sea ice¹⁶. For instance, Zhuo and Jiang (2020)¹⁷ demonstrated that 60% of winter sea ice decline in the Bering Sea is explained by the near-surface southeasterly winds and 40% by a subsequent change in the downward longwave radiation. The summertime moisture transport

was also found to strongly shape the sea ice area in the Arctic Pacific sector⁷. More globally, the importance of AMET in the current Arctic warming was documented in numerical experiments⁴ and in a modelling of an energy budget for possible future Arctic warming¹⁸.

In this study, we discovered a novel large-scale division of monthly internal energy transport at the latitude 70°N based on the analysis of empirical orthogonal functions applied to the longitude–height sections of the sensible and latent heat fluxes. According to radiosonde observations, these two fluxes are the major components and constitute more than 70% in the net energy transport into the Arctic⁶. The potential energy flux is not considered in this study.

Methods

Data

In this study, we used the ERA5 climate reanalysis at monthly temporal resolution for the period from January 1950 to December 2019. The reanalysis for the period 1950–1978 is only the preliminary version and is subject to changes yet due to unrealistically strong tropical cyclones, but the present era from 1979 is fully completed²⁶. As our focus is on the high-latitude processes, we assume that the current issues for 1950–1978 should not affect the results presented here. The following variables were downloaded:

1. Monthly mean meridional component of wind velocity (m s^{-1}) on the 27 isobaric surfaces 1000–100 hPa in the area 60°N–80°N with a horizontal resolution $1^\circ \times 1^\circ$ and vertical resolution 25–50 hPa (each available isobaric surface has been used). The highest spatial resolution $0.25^\circ \times 0.25^\circ$ was not used, as it is not critical for this part of study and allows saving computational resources.
2. Monthly mean meridional component of wind velocity (m s^{-1}) on the 27 isobaric surfaces 1000–100 hPa at the latitude 70°N with a horizontal resolution $0.25^\circ \times 0.25^\circ$ and vertical resolution 25–50 hPa.
3. Monthly mean air temperature (K) on the 27 isobaric surfaces 1000–100 hPa at the latitude 70°N with a horizontal resolution $0.25^\circ \times 0.25^\circ$ and vertical resolution 25–50 hPa.
4. Monthly mean specific humidity (kg kg^{-1}) on the 27 isobaric surfaces 1000–100 hPa at the latitude 70°N with a horizontal resolution $0.25^\circ \times 0.25^\circ$ and vertical resolution 25–50 hPa.
5. Monthly mean geopotential (m^2s^{-2}) on the 27 isobaric surfaces 1000–100 hPa at the latitude 70°N with a horizontal resolution $0.25^\circ \times 0.25^\circ$ and vertical resolution 25–50 hPa. These data were transformed to the geopotential heights (m) after dividing by the gravitational acceleration (9.80665 m s^{-2}).

Investigation of the monthly northward wind fields around the parallel 70°N

Here, we found the mean meridional component of wind velocity at every grid point for the region 60°N–80°N in the three atmospheric layers (1000–800 hPa, 775–400 hPa and 350–100 hPa), which is nine isobaric surfaces per layer. The monthly values were first averaged over the isobaric surfaces, and then

temporal means were found for 1950–1978 and 1979–2019, which is consistent with the ERA5 development and the known cooling and warming periods of the present climate^{27–29}. To determine the dominant wind directions in the Eastern and Western Hemispheres (0°–179°E and 180°–1°W, respectively), the area-weighted averages were computed for every obtained result according to the method in Greene et al., 2019³⁰.

Calculation of the monthly meridional sensible and latent heat transport (SHT and LHT) components through the latitude 70°N and their decomposition into the empirical orthogonal functions (EOFs)

The sensible (SHT) and the latent (LHT) heat transports (W m^{-2}) were computed as follows:

$$SHT_{l,p,t(70^\circ N)} = C_p \rho T_{l,p,t} V_{l,p,t} \quad (1)$$

$$LHT_{l,p,t(70^\circ N)} = L_v \rho Q_{l,p,t} V_{l,p,t}, \quad (2)$$

where C_p is the mean specific heat capacity of air at constant pressure equal to $1005 \text{ J kg}^{-1} \text{ K}^{-1}$, L_v is the mean latent heat of vaporization equal to $2.5 \times 10^6 \text{ J kg}^{-1}$, l is the longitude, p is the isobaric surface, t is time, ρ is the mean air density equal to 1.3 kg m^{-3} , T is the monthly mean air temperature (K), Q is the monthly mean specific humidity (kg kg^{-1}), V is the monthly mean northward wind velocity (m s^{-1}).

This method was used in Alekseev et al. (2019)¹¹, but that study had a regional focus in the Atlantic-European part. The equations (1) and (2) represent the instantaneous meridional fluxes because they are estimated for every longitude and isobaric surface at a given time. This approach provides much more detailed structure on the individual heat transport components than previous studies where these were computed from spatial (zonal and vertical) and time means³. To investigate large-scale features of heat fluxes, we decomposed the sensible and latent heat transports across 70°N (functions of longitude, isobaric surface, and time) into the empirical orthogonal functions (EOFs) following the techniques described in Greene et al., 2019³⁰. Therefore, the monthly time series were both detrended and deseasoned prior to the EOF analysis.

Investigation of the vertical distributions of the annual meridional sensible and latent heat transport (SHT and LHT) components through the latitude 70°N

The longitudinal averaging was done for the Eastern and Western Hemispheres (0°–179.75°E and 180°–0.25°W, respectively) because the EOF analysis suggested different variability in these regions. The noisy monthly time series were averaged for every year to highlight the vertical structure of heat fluxes in the entire troposphere 1000–100 hPa by means of time-altitude diagrams. The standard deviations were analyzed along the temporal and vertical dimensions (over the years and isobaric surfaces) to analyze

how the sensible and latent heat transports are controlled in the Eastern and Western Hemispheres. The annual means were used for this part of study only. In all other cases, monthly time series were analyzed.

Integral sensible and latent heat transports (SHT and LHT) in the lower and entire troposphere and their net fluxes through the Arctic gate

The monthly times series of sensible and latent heat transports were further integrated ($SHT_{int.}$ and $LHT_{int.}$, W) in both hemispheres for two atmospheric layers previously identified by the mean directions of fluxes: 1000–800 hPa and 1000–100 hPa as written in the equations (3) and (4):

$$SHT_{int.} = \int_{p_1}^{p_2} \int_{l_1}^{l_2} (SHT_{l,p,t(70^\circ N)}) dl dp \quad (3)$$

$$LHT_{int.} = \int_{p_1}^{p_2} \int_{l_1}^{l_2} (LHT_{l,p,t(70^\circ N)}) dl dp, \quad (4)$$

where p_1 and p_2 correspond to the layers 1000–800 hPa and 1000–100 hPa, l_1 and l_2 mark the limits of either the Eastern Hemisphere (0° – 179.75° E) or the Western Hemisphere (180° – 0.25° W), the horizontal integration step $dl = 0.25^\circ$, the vertical integration step $dp = 25$ or 50 hPa in accordance with the data on geopotential heights at each grid point corresponding to the isobaric surfaces. Numerical integration was carried out by the trapezoidal method.

In the time series obtained the mean values were calculated for every case, and the confidence interval for the uncertainties of the means was estimated based on the t -distribution for the 5% significance level³¹. Subsequently, the net sensible and latent heat transports were found by adding the time series in the Eastern and Western Hemispheres for every atmospheric layer. The obtained time series can be interpreted as the net heat fluxes for the given latitude (70° N). The internal energy budgets for the lower and entire troposphere were calculated by adding the sensible and latent heat fluxes in the hemispheres. Plotting of the monthly integral heat fluxes was done after applying the loess smoothing with a span of 5% of the values to smooth out high-frequency data and highlight the anti-phase pattern between the hemispheres. The interquartile ranges (differences between 75th and 25th percentiles) for each pair of the time series were computed for the unsmoothed monthly time series, and the corresponding shaded areas have been added to the curves. The Pearson correlation coefficients were computed for both unsmoothed and filtered time series displayed in the Figure.

Results

Mean meridional component of wind velocity in the atmospheric layers around 70°N

For any component of AMET, an essential variable is the northward wind velocity. Therefore, we first investigated the wind fields around the parallel 70°N (Fig. 1).

The three chosen layers represent the lower troposphere with a direct interaction with the Earth's surface, the middle troposphere with a steering flow and the upper troposphere, where the main jet streams are located. The fields are very similar for both periods and so we focus on the present period, 1979–2019. The calculation of AMET through the latitude 70°N is consistent with the meridional wind fields, as this parallel crosses the large areas of increased wind velocity near their cores.

The results show that the meridional winds of both directions are the strongest over North America and Greenland. In the lower troposphere, the winds of both directions are weak over Eurasia, and there is a steady northward direction (Fig. 1b). The most clear picture of the alternating wind directions arises in the upper troposphere (Fig. 1e-f). It seems natural dividing the region into two hemispheres separated by the prime meridian 0°: 0°–179°E and 180°–1°W. The area-weighted average wind velocities support this division. In the lower troposphere of the Eastern Hemisphere the winds are directed towards the Arctic (0.23 m s^{-1}), whereas in the Western Hemisphere, the southward wind direction prevails (-0.34 m s^{-1}). In the middle and upper troposphere, the situation is reversed: the northward winds prevail in the Western Hemisphere and southward winds prevail in the Eastern Hemisphere (0.36 m s^{-1} and 0.77 m s^{-1} versus -0.28 m s^{-1} and -0.65 m s^{-1} , respectively).

Analysis of empirical orthogonal functions for the time series of sensible and latent heat transport components and the resulting large-scale regional division

The time series of sensible and latent heat transports across 70°N (equations 1 and 2) were decomposed into empirical orthogonal functions (EOFs) (Fig. 2).

The leading modes of variability are nearly exactly divided into the Eastern and Western Hemispheres: variability of the sensible heat transport dominates in the Western Hemisphere, whereas that of the latent heat transport dominates in the Eastern Hemisphere. This division is more pronounced for the latent heat transport. The three EOFs in the figure explain about 50% of the variability for each heat transport component. The hemispheric pattern in the modes of variability is preserved if additional EOFs are added. For the sensible heat transport, the first eight EOFs explain 81% of the variance, and the first eight EOFs for the latent heat transport explain 79% of the variance. These results confirm the robustness of the identified hemispheric division for the components of the heat transport. The possible physical reasons are addressed further.

Anti-phase pattern in the sensible and latent heat transports between the Eastern and Western Hemispheres

In order to examine the vertical structure of sensible and latent heat transports, they were longitudinally averaged for the Eastern and Western Hemispheres. The noisy monthly time series were averaged to obtain annual means (Fig. 3a-d).

These time-altitude diagrams demonstrate the prevalence of sensible and latent heat transports into the Arctic in the lower troposphere (1000–800 hPa) and from the Arctic in the middle and upper troposphere for the Eastern Hemisphere. For the Western Hemisphere, the vertical distribution of the heat fluxes is opposite, which indicates a dipole anti-phase pattern between the hemispheres. According to the concept of the polar circulation cell¹⁹, heat transport should be directed into the Arctic in the upper troposphere and from the Arctic in the lower troposphere, which is true for the Western Hemisphere, but completely different in the Eastern Hemisphere. However, the anti-phase pattern is more stable for the sensible heat transport, because for the latent heat transport, there are layers with the same direction of fluxes in both hemispheres. For instance, these features are seen around 700–800 hPa (Fig. 3c-d).

The vertical cross-sections (Fig. 3a-d) show visually notable differences in the variability between the hemispheres, especially for the latent heat transport. Indeed, the interannual standard deviation averaged over the height of the troposphere (1000–100 hPa) is 0.61 kW m^{-2} for the latent heat transport in the Eastern Hemisphere and only 0.45 kW m^{-2} in the Western Hemisphere. This means the interannual variability of latent heat transport is 1.36 times higher in the Eastern Hemisphere than in the Western Hemisphere. For the sensible heat transport, the interannual variability is comparable, being 68.45 kW m^{-2} in the Western Hemisphere and 71.53 kW m^{-2} in the Eastern Hemisphere, which is only 1.05 times higher. However, the temporal mean of the standard deviations over the isobaric surfaces reveals the dominance of sensible heat transport in the Western Hemisphere because it is 192.7 kW m^{-2} here versus 130.97 kW m^{-2} in the Eastern Hemisphere. This means the variability of sensible heat transport over the isobaric surfaces is 1.47 times higher in the Western Hemisphere than in the Eastern Hemisphere, which is also supported by a stronger vertical colour gradient in Fig. 3b than in Fig. 3a. The same estimates for the latent heat transport give a value of 1.35 kW m^{-2} for the Western Hemisphere and 1 kW m^{-2} for the Eastern Hemisphere. This means the variability of latent heat transport over the isobaric surfaces is 1.35 times higher in the Western Hemisphere than in the Eastern Hemisphere.

Thus, the hemispheric division based on the modes of variability in Fig. 2 corresponds to the highest ratios in the standard deviations (1.36 and 1.47). Whether the variability with time or height (isobaric surfaces) dominates the overall variability in latent heat transport and sensible heat transport depends upon the hemisphere. A more clear division into the Eastern and Western Hemispheres in Fig. 2 for the latent heat transport might be due to a higher overall importance of interannual standard deviations at different isobaric surfaces compared to standard deviations over isobaric surfaces for every year.

Fully integrated sensible and latent heat transports in the lower and entire troposphere and their net values through the Arctic gate

The monthly integral sensible and latent heat transports in the lower troposphere (1000–800 hPa) and the entire troposphere (1000–100 hPa) were studied (Fig. 4). The layers were identified based on the previous results on the mean directions of heat fluxes (Fig. 3).

The loess smoothing was applied to demonstrate the anti-phase pattern between the hemispheres (Fig. 4a-d) and the sign of the net fluxes (Fig. 4e-f). For the sensible heat transport in the entire troposphere (Fig. 4a and e), heat transport is mostly directed into the Arctic due to a stronger mean heat influx in the Western Hemisphere than heat outflux in the Eastern Hemisphere. The correlation coefficients for the unsmoothed time series used in the Fig. 4a are -99.68% and -99.56% for the smoothed time series displayed in the Fig. 4a. For the sensible heat transport in the lower troposphere (Fig. 4c and e), heat transport is mostly directed away from the Arctic due to a weaker mean heat influx in the Eastern Hemisphere than heat outflux in the Western Hemisphere. Thus, in the lower troposphere, the direction of heat fluxes in the hemispheres is flipped. The correlation coefficients for the unsmoothed time series used in the Fig. 4c are -88.18% and -79.85% for the smoothed time series displayed in the Fig. 4c.

For the latent heat transport in the entire troposphere (Fig. 4b and f), heat transport is mostly directed into the Arctic due to a combined effect of mean positive heat influxes in the Eastern and Western Hemispheres. This is also confirmed by a large area of intersection for the interquartile ranges in Fig. 4b and by significantly higher absolute values for the 75th percentiles than for the 25th percentiles. However, the clearly seen anti-phase pattern is preserved, and the correlation coefficients for the unsmoothed time series used in the Fig. 4b are -82.07% and -77.02% for the smoothed time series displayed in the Fig. 4b. For the latent heat transport in the lower troposphere (Fig. 4d and f), heat transport is also mostly directed into the Arctic, but due to a stronger mean heat influx in the Eastern Hemisphere than heat outflux in the Western Hemisphere. The correlation coefficients for the unsmoothed time series used in the Fig. 4d are -65.65% and -53.67% for the smoothed time series displayed in the Fig. 4d.

The internal energy budgets defined by the sums of sensible and latent heat fluxes between the hemispheres are -0.65 ± 0.09 PW for the lower troposphere 1000–800 hPa and 4.28 ± 0.18 PW in the entire troposphere 1000–100 hPa. In both cases, the overall sign is defined by the several orders of magnitude higher absolute values of sensible heat flux than of latent heat flux. The mean values and corresponding uncertainties for the intermediate cases are shown in the Table 1.

Table 1. Mean heat fluxes of sensible heat transport (SHT) and latent heat transport (LHT) for the Eastern Hemisphere (EH) and Western Hemisphere (WH).

	SHT, PW (10^{15} W)		LHT, TW (10^{12} W)	
	EH	WH	EH	WH
1000–800 hPa	1.35 ± 0.19	-2.02 ± 0.17	19.98 ± 3.83	-13.16 ± 2.64
1000–100 hPa	-11.14 ± 2.11	15.38 ± 2.17	18.01 ± 7.15	24.75 ± 6.40
Net flux (1000–800 hPa)	-0.66 ± 0.09		6.81 ± 2.89	
Net flux (1000–100 hPa)	4.24 ± 0.18		42.75 ± 4.12	

Discussion And Conclusions

This study has revealed the dipole pattern of the meridional sensible and latent heat transports into the Arctic between the Eastern and Western Hemispheres. This pattern is pronounced in the different variability and anti-phase feature between the hemispheres. The physical significance of the large-scale hemispheric division obtained from the EOF analysis across the zonal section at 70°N has been confirmed by the analysis of time-altitude diagrams in the areas longitudinally averaged for the Eastern Hemisphere and Western Hemisphere, fully integrated sensible and latent heat transports and the net of these transports. The latent heat transport is a major contributor to the heat excess into the Arctic. For this component, the net heat flux is positive both in the lower and in the entire troposphere.

What might explain the dominance of latent heat transport in the Eastern Hemisphere and sensible heat transport in the Western Hemisphere? This requires further in-depth studies; however, we think the exact clues are hidden in the following conceptual explanation. Regarding the dominance of latent heat transport in the Eastern Hemisphere, first, the extratropical cyclones, originating in the North Atlantic, carry moisture to the northeast, thus affecting the Arctic in the western and central parts of the Eastern Hemisphere^{20–22}. Second, the cyclone tracks from the North Pacific are predominantly directed northwest²³, thus affecting the Arctic in the far eastern area of the Eastern Hemisphere. Third, the Siberian atmospheric rivers are responsible for the dominance of latent heat transport in the central and eastern part of the Eastern Hemisphere²⁴. The three different processes work simultaneously and give rise to the large-scale convergence of the moisture transport into the Arctic in the Eastern Hemisphere. According to the results of our study, the dominance of sensible heat transport in the Western Hemisphere is over the isobaric surfaces 1000–100 hPa. This might be related to the trend in the cold air outbreaks, which has a pronounced negative sign in the Western Hemisphere according to the ERA5 reanalysis; at the same time, the frequency and magnitude of cold air outbreaks in the Eastern Hemisphere have not changed significantly since 1979²⁵.

Declarations

Data Availability

The ERA5 reanalysis data used in this study are publicly available from the Copernicus Climate Change Service: <https://climate.copernicus.eu/climate-reanalysis>.

Code Availability

The MATLAB codes used for the calculations and creation of Figures discussed in this work have been archived and are available on request from the corresponding author, M.M.L. (m.m.latonin@spbu.ru).

Acknowledgements

This study was funded by the Russian Foundation for Basic Research (RFBR), project number 19-35-90083. We also acknowledge the financial support of the Nansen Environmental and Remote Sensing Center (NERSC), Bergen, Norway. In addition, R.D. acknowledges the project KeyCLIM funded by the Norwegian Research Council, project number 295046. M.M.L. is also grateful to the support of the Nansen Scientific Society (Bergen, Norway).

Author Contributions

M.M.L. has conceptualized the work and written an original article draft. L.P.B., I.L.B. and R.D. have jointly supervised the work and edited the article.

Competing Interests

The authors declare no competing interests.

References

1. Semmler, T., Jacob, D. & Schlunzen, K. H. The water and energy budget of the Arctic atmosphere. *J. Clim*, **18**, 2515–2530 (2005).
2. Serreze, M. C., Barrett, A. P. & Slater, A. G. The large-scale energy budget of the Arctic. *J. Geophys. Res*, **112**, D11122 (2007).
3. Overland, J. E., Turet, P. & Oort, A. H. Regional variations of moist static energy flux into the Arctic. *J. Clim*, **9**, 54–65 (1996).
4. Yoshimori, M., Abe–Ouchi, A. & Laîné, A. The role of atmospheric heat transport and regional feedbacks in the Arctic warming at equilibrium. *Clim. Dyn*, **49**, 3457–3472 (2017).
5. Dufour, A., Zolina, O. & Gulev, S. K. Atmospheric moisture transport to the Arctic: assessment of reanalyses and analysis of transport components. *J. Clim*, **29**, 5061–5081 (2016).
6. Sorokina, S. A. & Esau, I. N. Meridional energy flux in the Arctic from data of the radiosonde archive IGRA. *Izvestiya, Atmospheric and Oceanic Physics*, **47**, 572–583 (2011).
7. Lee, H. J. *et al.* Impact of poleward moisture transport from the North Pacific on the acceleration of sea ice loss in the Arctic since 2002. *J. Clim*, **30**, 6757–6769 (2017).

8. Xu, D., Du, L., Ma, J. & Shi, H. Pathways of meridional atmospheric moisture transport in the Central Arctic. *Acta Oceanol. Sin*, **39**, 55–64 (2020).
9. Kim, H., Yeh, S. W., An, S. I. & Song, S. Y. Changes in the role of Pacific Decadal Oscillation on sea ice extent variability across the mid–1990s. *Sci. Rep*, **10**, 17564 (2020).
10. Graham, R. M. *et al.* Increasing frequency and duration of Arctic winter warming events. *Geophys. Res. Lett*, **44**, 6974–6983 (2017).
11. Alekseev, G., Kuzmina, S., Bobylev, L., Urazgildeeva, A. & Gnatiuk, N. Impact of atmospheric heat and moisture transport on the Arctic warming. *Int. J. Climatol*, **39**, 3582–3592 (2019).
12. Jakobson, E. & Vihma, T. Atmospheric moisture budget in the Arctic based on the ERA-40 reanalysis. *Int. J. Climatol*, **30**, 2175–2194 (2010).
13. Vázquez, M. *et al.* Atmospheric rivers over the Arctic: Lagrangian characterisation of their moisture sources. *Water*, **11**, 41 (2019).
14. Thompson, D. W. J. & Wallace, J. M. The Arctic Oscillation signature in the wintertime geopotential height and temperature fields. *Geophys. Res. Lett*, **25**, 1297–1300 (1998).
15. Van der Swaluw, E., Drijfhout, S. & Hazeleger, W. Bjerknes compensation at high northern latitudes: the ocean forcing the atmosphere. *J. Clim*, **20**, 6023–6032 (2007).
16. Mortin, J. *et al.* Melt onset over Arctic sea ice controlled by atmospheric moisture transport. *Geophys. Res. Lett*, **43**, 6636–6642 (2016).
17. Zhuo, W. & Jiang, Z. A possible mechanism for winter sea ice decline over the Bering Sea and its relationship with cold events over North America. *J. Meteor. Res*, **34**, 575–585 (2020).
18. Alexeev, V. A. & Jackson, C. H. Polar amplification: is atmospheric heat transport important? *Clim. Dyn*, **41**, 533–547 (2013).
19. Rossby, C. G. & Willett, H. C. The circulation of the upper troposphere and lower stratosphere. *Science*, **108**, 643–652 (1948).
20. Hurrell, J. W. Decadal trends in the North Atlantic Oscillation: Regional temperatures and precipitation. *Science*, **269**, 676–679 (1995).
21. Rinke, A. *et al.* Extreme cyclone events in the Arctic: Wintertime variability and trends. *Environ. Res. Lett*, **12**, 094006 (2017).
22. Wickström, S., Jonassen, M. O., Vihma, T. & Uotila, P. Trends in cyclones in the high-latitude North Atlantic during 1979–2016 (2019). *Q. J. R. Meteorol. Soc*, **146**, 762–779 (2019).
23. Sorteberg, A. & Walsh, J. E. Seasonal cyclone variability at 70°N and its impact on moisture transport into the Arctic. *Tellus A*, **60**, 570–586 (2008).
24. Komatsu, K. K., Alexeev, V. A., Repina, I. A. & Tachibana, Y. Poleward upgliding Siberian atmospheric rivers over sea ice heat up Arctic upper air. *Sci. Rep*, **8**, 2872 (2018).
25. Smith, E. T. & Sheridan, S. C. Where do cold air outbreaks occur, and how have they changed over time? *Geophys. Res. Lett*, **47**, e2020GL086983 (2020).
26. Hersbach, H. *et al.* The ERA5 global reanalysis. *Q. J. R. Meteorol. Soc*, **146**, 1999–2049 (2020).

27. Rogers, J. C. The 20th century cooling trend over the southeastern United States. *Clim. Dyn*, **40**, 341–352 (2013).
28. Hodson, D. L. R., Robson, J. I. & Sutton, R. T. An anatomy of the cooling of the North Atlantic Ocean in the 1960s and 1970s. *J. Clim*, **27**, 8229–8243 (2014).
29. Rahmstorf, S., Foster, G. & Cahill, N. Global temperature evolution: Recent trends and some pitfalls. *Environ. Res. Lett*, **12**, 054001 (2017).
30. Greene, C. A. *et al.* The climate data toolbox for MATLAB. *Geochem. Geophys*, **20**, 3774–3781 (2019).
31. Wilks, D. S. *Statistical Methods in the Atmospheric Sciences, second ed* (International Geophysics Series, San Diego, CA, USA, 2006).

Figures

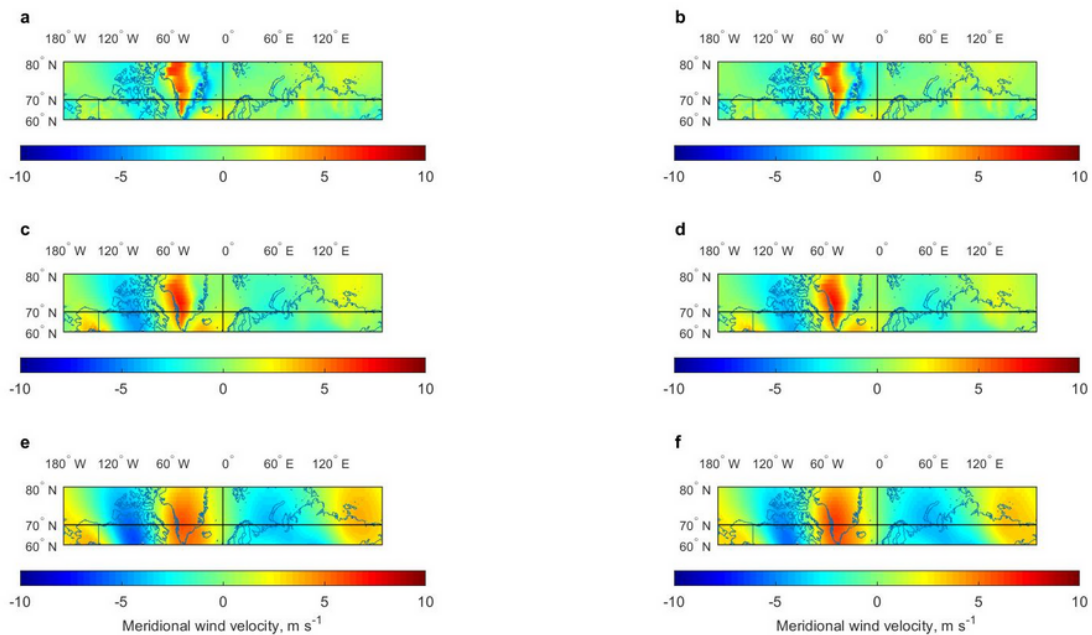


Figure 1

Mean meridional component of wind velocity (m s^{-1}) for the region 60° – 80° N in the different atmospheric layers averaged for 1979–2019 (left) and 1950–1978 (right). a, 1979–2019 and 1000–800 hPa. b, 1950–1978 and 1000–800 hPa. c, 1979–2019 and 775–400 hPa. d, 1950–1978 and 775–400 hPa. e, 1979–2019 and 350–100 hPa. f, 1950–1978 and 350–100 hPa. Positive values indicate northward direction. The reference lines are drawn at the 70° N and prime meridian 0° . Mercator map projection is used. The Matrix Laboratory (MATLAB) with version R2017b (<https://www.mathworks.com/>) was used to generate this Figure.

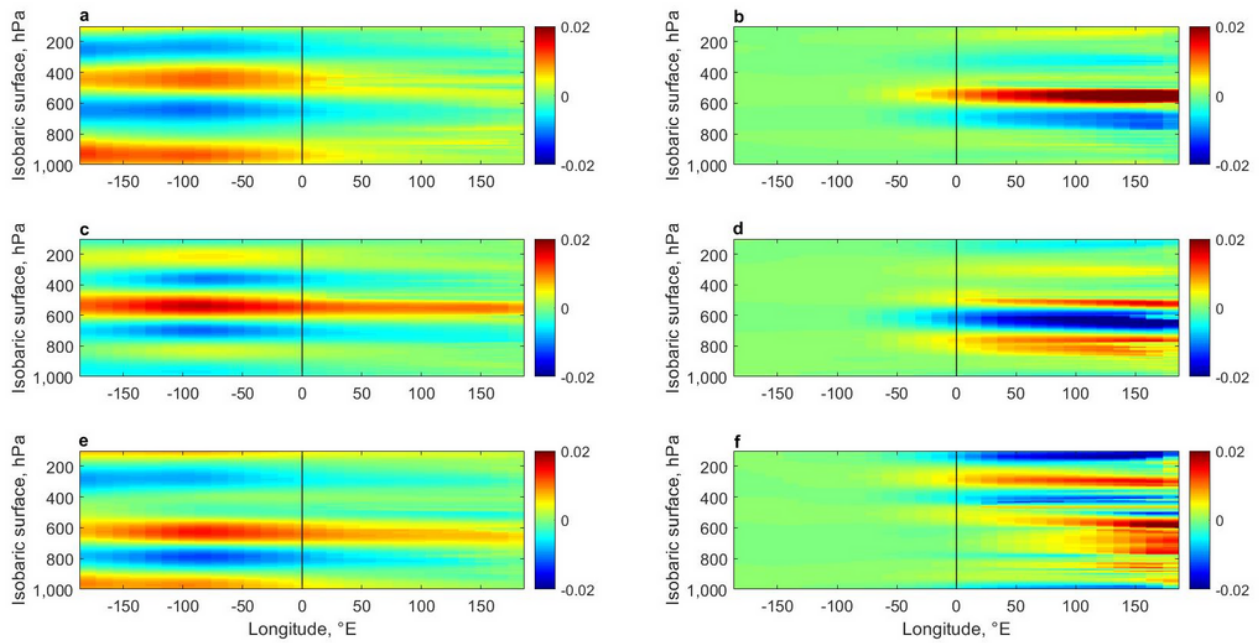


Figure 2

Empirical orthogonal functions (EOFs) of the sensible (left) and latent (right) heat transport components (SHT and LHT). a, First EOF for the SHT (21.7%). b, First EOF for the LHT (23.8%). c, Second EOF for the SHT (15.4%). d, Second EOF for the LHT (14.7%). e, Third EOF for the SHT (12.6%). f, Third EOF for the LHT (12.6%). The reference lines are drawn at the prime meridian 0°. The values in the parentheses are the fractions of variance explained by each mode. The Matrix Laboratory (MATLAB) with version R2017b (<https://www.mathworks.com/>) was used to generate this Figure.

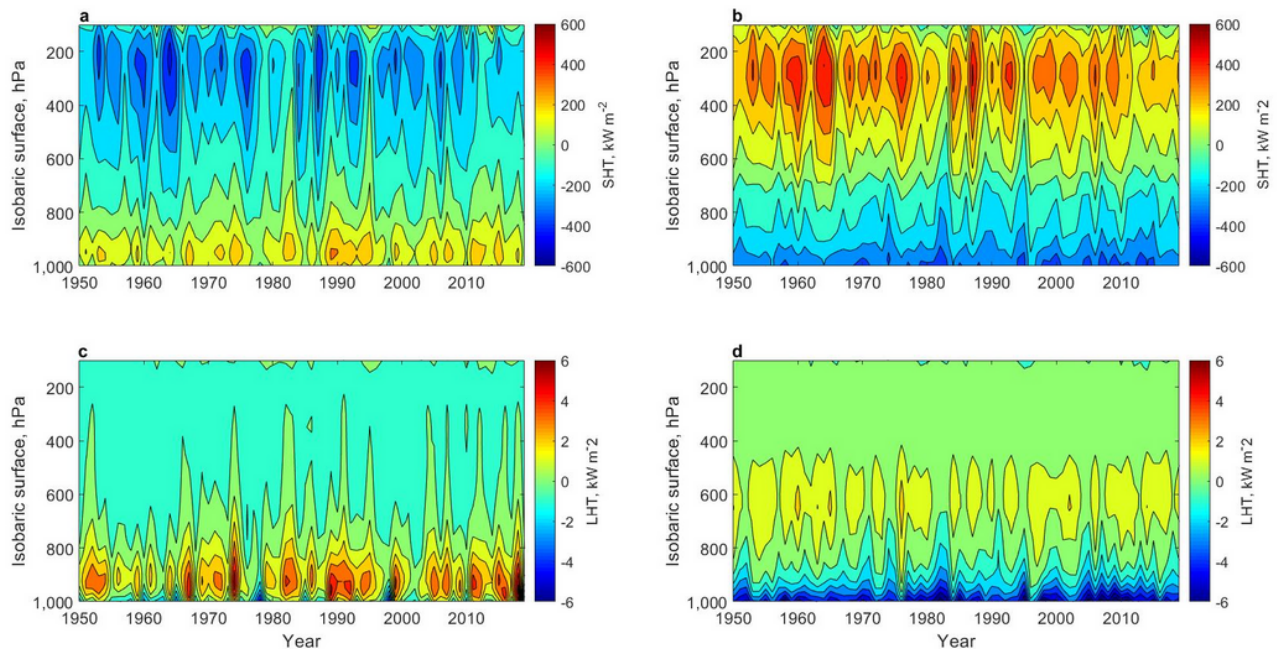


Figure 3

Vertical cross-section of heat transport components (kW m^{-2}), their interannual variability and the anti-phase pattern between the hemispheres. a, Annual average sensible heat transport in the Eastern Hemisphere ($0^\circ - 179.75^\circ\text{E}$). b, Annual average sensible heat transport in the Western Hemisphere ($180^\circ - 0.25^\circ\text{W}$). c, Annual average latent heat transport in the Eastern Hemisphere ($0^\circ - 179.75^\circ\text{E}$). d, Annual average latent heat transport in the Western Hemisphere ($180^\circ - 0.25^\circ\text{W}$). The positive values indicate northward heat transport. The Matrix Laboratory (MATLAB) with version R2017b (<https://www.mathworks.com/>) was used to generate this Figure.

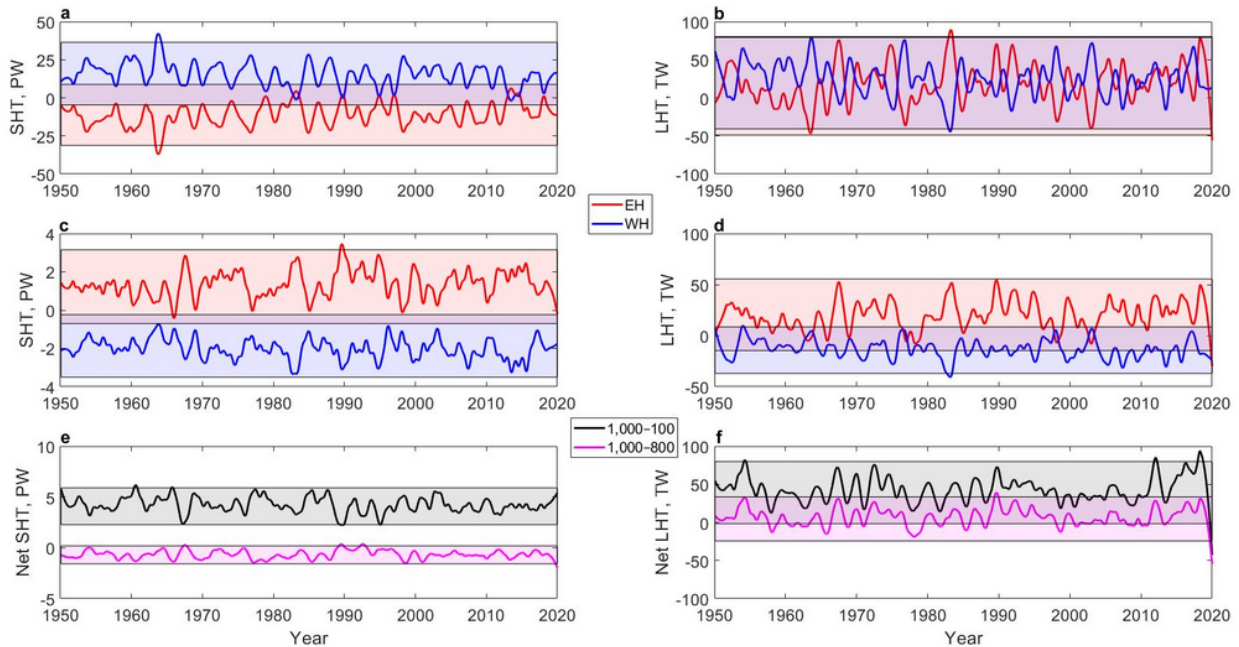


Figure 4

Smoothed time series of integral sensible and latent heat transport (SHT and LHT) components (Petawatt (PW) and Terawatt (TW)) in the lower and entire troposphere for the Eastern and Western Hemispheres (EH and WH) and the net fluxes. a, 1000–100 hPa integral SHT in the EH and WH. b, 1000–100 hPa integral LHT in the EH and WH. c, 1000–800 hPa integral SHT in the EH and WH. d, 1000–800 hPa integral LHT in the EH and WH. e, Net fluxes of SHT (EH + WH). f, Net fluxes of LHT (EH + WH). The lighter shaded areas indicate the interquartile ranges (differences between 75th and 25th percentiles) for the unsmoothed monthly time series, and the darker shaded areas show the intersections of the interquartile ranges for each pair of the time series. The loess smoothing was performed with a span of 5% of the values. The Matrix Laboratory (MATLAB) with version R2017b (<https://www.mathworks.com/>) was used to generate this Figure.